Energy & Environmental Science

ROYAL SOCIETY OF CHEMISTRY

PAPER

View Article Online
View Journal | View Issue

Cite this: *Energy Environ. Sci.*, 2022, **15**, 3086

Vapor and heat dual-drive sustainable power for portable electronics in ambient environments†

Jiaxin Bai,[a] Yajie Hu,[b] Tianlei Guang,[a] Kaixuan Zhu,[a] Haiyan Wang,[b] Huhu Cheng,[ab] Feng Liu[c] and Liangti Qu *[ab]

Received 15th March 2022,
Accepted 24th May 2022

DOI: 10.1039/d2ee00846g

rsc.li/ees

Ubiquitous vapor and low-grade heat are widely available in nature and provide abundant, clean sources for developing new types of power generators. Herein, we demonstrate high-performance power, driven by vapor and heat for portable electronics in ambient environments. Based on the ternary aggregate of a polyelectrolyte, conducting polymer and a redox couple, the vapor and heat dual-drive electric generator (VHG) of 1 cm^2 offers an open circuit voltage of 0.9 V, and a sustainable short-circuit-current density of up to 0.8 mA cm^{-2}, much higher than that of single-source generators. Resulting from synergistic double-acting ion migration and the thermogalvanic effect, the high-efficiency VHG can work as a flexible personal energy-supply system to support wearable devices, such as hearing aids, by using body sweat and heat. It can even light a 15 W bulb once compatibly installed in a greenhouse. This work paves the way for sustainable energy generation by effectively collecting multiple types of natural energy comprehensively to realize sustainable applications in different seasons and geographical locations.

Broader context

Environmental energy conversion technologies have attracted enormous social interest for satisfying the great demands of electric power. Accordingly, significant advances have been made to convert only one form of environmental energy, including solar radiation, wind power, bioenergy and mechanical energy, into electricity. Other concurrent clean sources are regrettably neglected. Therefore, obtaining multiple clean sources for driving a hybrid device is a significant challenge in the upgrade of energy converting systems. In nature, ubiquitous vapor and low-grade heat provide abundant clean sources for developing new types of power generators. In this study, we develop a high-performance vapor and heat dual-drive electric generator (VHG) that spontaneously harvests concomitant vapor and heat from the environment in a consistent direction for efficient electric output. A 1 cm^2 VHG unit offers an open circuit voltage of 0.9 V, and a considerable short-circuit-current density of up to 0.8 mA cm^{-2}. This high current density is much higher than that of most single-source generators based on vapor or heat, resulting from the combination of double-acting ion migration and the thermogalvanic effect. The flexible VHGs can work as personal energy supply systems in various real natural scenarios for different seasons for powering electricity-consuming devices.

Introduction

Spontaneous power generation technologies have been developed to satisfy the enormous demands of electric power for electronics in daily life, from the communication industry to agriculture.[1] Great efforts in power engineering projects, including solar cells,[2] wind turbines,[3] piezoelectric/triboelectric nanogenerators,[4,5] and microbial cells,[6] have been devoted to converting environmental energy into electricity.

In nature, abundant clean sources occur concurrently, and this provides new opportunities for developing hybrid power generators in real natural conditions. For example, the ubiquitous aqueous vapor is constantly concomitant with low-grade heat sources (<100 °C), which are widely available in the natural environment, living things and agricultural industry.[7,8] In ordinary atmospheric moisture-enabled electric generation, water adsorption serves as the single driving force to induce ion diffusion directionally for electric generation.[9–11] Such insufficient ion migration triggers the unsatisfactory current density of the device unit. The difficulty also lies in the heavy dependence of the output on high relative humidity (RH) and special environmental requirements under artificial conditions in the laboratory.

[a] State Key Laboratory of Tribology, Department of Mechanical Engineering, Tsinghua University, Beijing, 100000, China. E-mail: lqu@mail.tsinghua.edu.cn
[b] Key Laboratory of Organic Optoelectronics & Molecular Engineering, Ministry of Education, Department of Chemistry, Tsinghua University, Beijing, 100000, China
[c] State Key Laboratory of Nonlinear Mechanics, Institute of Mechanics, Chinese Academy of Sciences, Beijing 100190, China

† Electronic supplementary information (ESI) available. See DOI: https://doi.org/10.1039/d2ee00846g

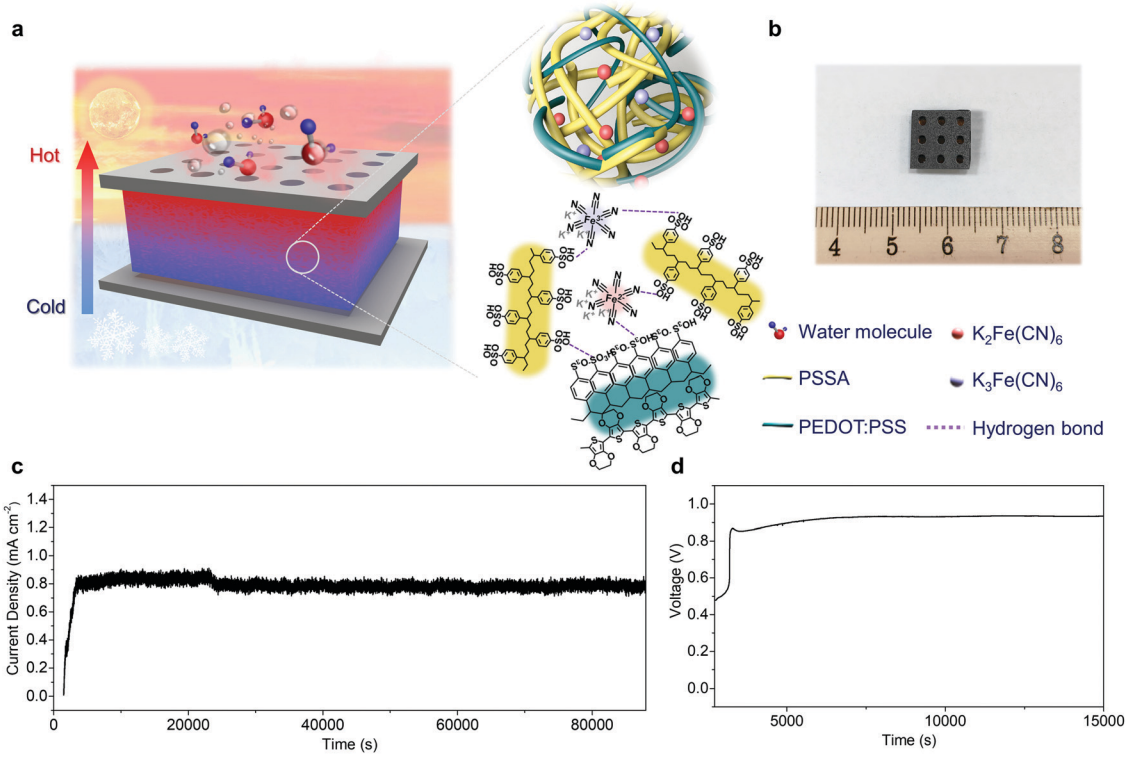

Fig. 1 Prototype of the VHG and the corresponding electric output. (a) A well-designed VHG synchronously driven by vapor and heat. The porous electrode is beneficial for vapor absorption and exposed to the hot surrounding, and the other electrode is sealed and regarded as the cold side of the VHG. The ternary electricity-generating layer is composed of PSSA matrix and additional PEDOT:PSS, $K_4Fe(CN)_6/K_3Fe(CN)_6$. (b) A photograph of the VHG unit. (c) and (d) I_{sc} output and V_{oc} output of the VHG under constant RH = 70%, and ΔT = 10 °C.

Thermal gradient provides another appropriate driving force for generating electricity based on the Soret effect.[12,13] Therefore, the synergetic utilization of low-grade heat and vapor to generate electricity is an ideal strategy for advanced power generation under complex and mutable conditions in nature. However, it remains an open question whether the vapor-induced effect and ionic thermoelectric effect could work together synergistically to boost the final power output in a hybrid system because of their fundamentally different physical pictures.

Herein, we propose a vapor and heat dual-drive electric generator (VHG), which synchronously harvests aqueous vapor and low-grade heat in a consistent direction for highly efficient electricity generation in natural scenarios (Fig. 1(a)). The VHG can produce a stable open-circuit voltage of up to 0.94 V and a high short-circuit current density of 0.8 mA cm^{-2} at RH of 70% and a temperature difference (ΔT) of 10 °C. The considerable performance results from the synergistic combination of double-acting ion migration and the thermogalvanic effect by adopting a ternary assembly consisting of hydrophilic polyelectrolyte, conducting polymer and a redox couple as verified by molecular dynamics simulations and Monte Carlo calculations. Compared with ordinary single-source generators, the vapor and thermal differences are fully utilized by the hybrid VHG for enhanced power output. The scalable integration of flexible and tailorable VHGs can work in various environments (10–80 °C, 30–90% RH), such as the sea, forest, and land from summer to winter without environmental restriction. The wearable VHGs can even generate more than 3 V based on human body sweat and heat, and supply enough power to drive commercial electricity-consuming devices in complex natural environments.

Results and discussion

Characterization and electrical performance of the VHG

The electricity-generating film consists of poly(4-styrenesulfonic acid), poly(3,4-ethylenedioxythiophene)-poly(styrenesulfonate) and $K_4Fe(CN)_6/K_3Fe(CN)_6$ (abbreviated as PSSA-PEDOT:PSS-$FeCN^{4-/3-}$). Briefly, PSSA with abundant hydrophilic functional groups (*i.e.*, $-SO_3H$) plays a role in water absorption and mobile H^+ ions dissociation in response to vapor.[14] PSSA/PEDOT:PSS serves as the ion provider for thermodiffusion.[15] $FeCN^{4-/3-}$, as a redox couple, undergoes reversible reactions under a temperature difference.[16] The free-standing film was fabricated by the simple drop-casting of their dispersion onto the desired substrates, followed by drying and peeling off. The ternary components were uniformly distributed in a quasi-solid-state composite (Fig. S1, ESI†).

To develop VHG for electrical measurements, the electricity-generating layer was sandwiched between two graphite electrodes (Fig. 1(a) and (b)). The upper electrode was porous to

ensure the effective access of the vapor to electricity-generating film. The bottom electrode and all the remaining parts were sealed (Fig. S2, ESI†). The VHG unit can generate the short-circuit current density (I_{sc}) of 0.72–0.86 mA cm^{-2} and work continuously for about 24 hours at RH = 70% and ΔT = 10 °C, reflecting its outstanding power-generating stability (Fig. 1(c)). The open-circuit voltage (V_{oc}) reached a maximum value of *ca.*0.94 V (Fig. 1(d)). These performances were repeatable for long-term testing (Fig. S3 and S4, ESI†). When the vapor approached the VHG, a power density of 6 μW cm^{-2} was detected (RH = 70%, 25 °C, Fig. S5, ESI†). Intriguingly, its amplitude further increased to 72 μW cm^{-2} upon RH = 70% and ΔT = 10 °C with 1100% enhancement (Fig. 2(a) and Fig. S6, ESI†). In addition, the configuration of film sandwiched with similar inert electrodes such as Au, Pt, and carbon tape, also yielded a favorable electric output (Fig. S7, ESI†).

The appropriate component content and thickness of the hybrid film are essential to the electric performance of the VHG (Fig. S8, ESI†). A considerable I_{sc} (0.8 mA cm^{-2}) of the ternary hybrid was optimized at a ratio of PSSA (92 wt%):PEDOT:PSS (7 wt%):FeCN$^{4-/3-}$ (1 wt%) with a film thickness of about 740 μm. The dependence of I_{sc} on RH (30–90%) demonstrates that power generation is directly related to the hydration level of the film exposed to a humid environment (Fig. S9, ESI†). Even at a low RH of 30%, VHG can proactively deliver a high I_{sc} of 0.1 mA cm^{-2}. Under high RH, the electric output of VHG was visibly enhanced due to the beneficial water adsorption ability and ion dissociation. In addition, the H^+ ion thermodiffusion induced by temperature difference will also be spurred under higher RH because water penetration will promote ion transport.[34,35] Fig. 2(b) shows the temperature dependence of the current performance over a range of ΔT from −10 °C to 30 °C

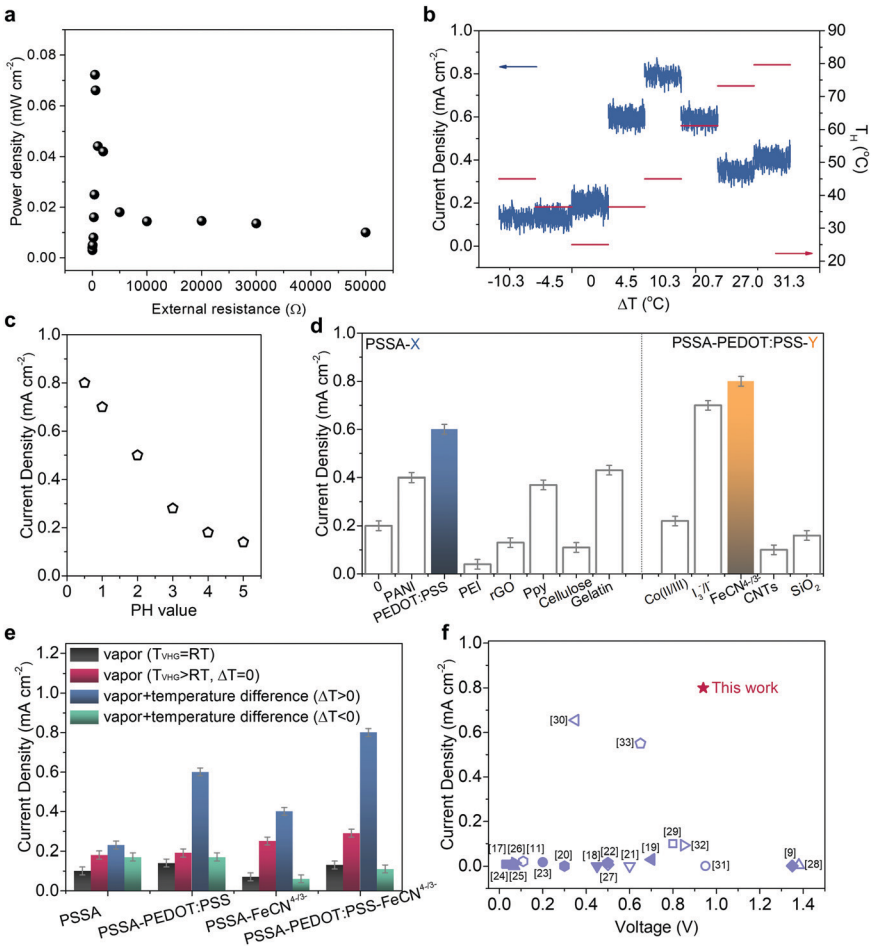

Fig. 2 Electric generation of a VHG unit. (a) Electric output of VHG with different electrical resistance as load. (b) I_{sc} of VHG under different ΔT at RH = 70%. ΔT = T_{upper} − T_{bottom}. T_{upper}: the temperature of upper electrode, T_{bottom}: the temperature of bottom electrode. T_H: the temperature of the electrode at hot side. (c) I_{sc} of VHG, with varying pH values of PSSA-PEDOT:PSS-FeCN$^{4-/3-}$ tuned by KOH. (d) I_{sc} of different hybrid films based on PSSA and additives (PSSA-X or PSSA-X-Y) under RH = 70% and ΔT = 10 °C. X: polyaniline (emeraldine base) (PANI), PEDOT:PSS, ethylene imine polymer (PEI), reduced graphene oxide (rGO), polypyrrole (Ppy), cellulose, gelatin. Y: cobalt(II/III) tris(bipyridyl) (Co(II/III)), iodide/triiodide (I^-/I_3^-), FeCN$^{4-/3-}$, carbon nanotube (CNTs), SiO_2 nanoparticles. (e) I_{sc} of PSSA, PSSA-PEDOT:PSS, PSSA-FeCN$^{4-/3-}$ and PSSA-PEDOT:PSS-FeCN$^{4-/3-}$ film upon vapor only (T_{VHG} = RT), vapor with uniform heating (T_{VHG} > RT, ΔT = 0), vapor + temperature difference (ΔT > 0 and ΔT < 0), respectively. The average temperature of VHGs are the same (35 °C) under ΔT = 0 (T_{VHG} > RT), ΔT > 0 and ΔT < 0. T_{VHG}: temperature of VHG. RT: room temperature. (f) A performance comparison of the typical water adsorption enabled electric generators reported for various macroscopic devices with inert electrodes (Table S1, ESI†).[9,11,17–33]

(Fig. S10, ESI†) at RH of 70%. At a specific ΔT of 10 °C, VHG realized a maximum value of 0.8 mA cm^{-2}, due primarily to the balanced water molecule adsorption and ion transport at an appropriate temperature, which is quite similar to that of the calculated current in Supplementary note 1 (ESI†). Moreover, the pH value highly affects the power generation of the VHG due to the ionization of functional groups (–SO_3H) in PSSA (Fig. 2(c)). When the pH was increased, the suppressed I_{sc} was observed because of impeded H^+ ion transfer, which verifies that the electric generation in VHG is strongly associated with the process of H^+ ion migration.

In the ternary hybrid film of PSSA-PEDOT:PSS-$FeCN^{4-/3-}$, PSSA has been explored for electric generation in previous research based on either water adsorption[29] or temperature difference configuration[36] separately. PEDOT:PSS[37] and $FeCN^{4-/3-}$ [38] respectively exhibited thermoelectric performances. Notably, the I_{sc} of VHG based on the composite film (0.8 mA cm^{-2}) is considered superior to that of the single component of PSSA film (0.2 mA cm^{-2}) under vapor accompanied by temperature difference. The vapor and heat dual-drive power effects of other additive species were also assessed (Fig. 2(d) and Fig. S11, ESI†). These polymers, redox couples and nanomaterials have been previously reported for their thermopower effects.[39–44] For all the comparable VHGs, the device based on PSSA, PEDOT:PSS and $FeCN^{4-/3-}$ appears to be the optimal construction for power generation. We propose that the impacts of different additives on I_{sc} are related to their water adsorption ability, ionic conductivity, and the coupling effect between them, which are discussed in detail in Supplementary note 2 (ESI†).

To confirm the specific influence of vapor and temperature difference, vapor only (T_{VHG} = RT), vapor with uniform temperature (T_{VHG} > RT, ΔT = 0), and temperature difference with different directions (ΔT > 0 and ΔT < 0) were applied separately to a VHG (Fig. S12, ESI†). The I_{sc} reached a maximum value of *ca.* 0.13 mA cm^{-2} solely with incoming vapor (RH = 70%), which is comparable to the reported single source generators (Fig. S13, ESI†).[29] This vapor-induced I_{sc} increased to 0.29 mA cm^{-2} under uniform heating (Fig. 2(e) and Fig. S14a, ESI†), and it further increased to 0.86 mA cm^{-2} under a temperature difference (ΔT > 0, Fig. S14b, ESI†). The enhancement in I_{sc} was achievable only when the gradient of water adsorption and temperature were in the same direction. Control studies of employing a temperature difference with ΔT < 0, namely the bottom electrode with higher temperature, yielded negligible performance (Fig. 2(e) and Fig. S14d, ESI†). In addition, a VHG based on two opposite porous electrodes produced a poor I_{sc} of 0.02 mA cm^{-2} (RH = 70% and ΔT = 10 °C, Fig. S15, ESI†) because the absence of a water adsorption gradient reduced the directional ion migration. It revealed that the configuration of VHG is superior to common thermo-induced electric generators. These results verify the synergistic effect of directional vapor adsorption and temperature difference in VHG. After systematic adjustments were made to the device structure and surrounding conditions, the VHG exhibited the optimal I_{sc} of 0.86 mA cm^{-2} under RH = 70% and ΔT = 10 °C. As illustrated in Fig. 2(f) and Tables S1, S2, ESI,† the output performance of VHG was much higher than that of most power-generating devices reported previously based on either water adsorption or temperature difference under the same conditions.[9,11,12,14,16–30,32–34,36,38,40,41,43–61]

Mechanism verification

The mechanism of vapor and heat dual-drive power could be proposed as follows. When vapor approaches the film through the porous upper electrode, the sulfonate groups in PSSA will spontaneously dissociate and release moveable H^+ ions (Fig. 3(a)).[29] Based on the vapor insulation on the bottom electrode and all remaining sides (Fig. S16, ESI†), the different hydration levels between the upper and bottom sides of the film lead to the gradient distribution of H^+ ions across the PSSA-PEDOT:PSS-$FeCN^{4-/3-}$ film, which will drive free H^+ ions to directionally move with water penetration deep into the film. In contrast, the negatively charged –SO_3^- groups anchored onto polymer skeletons are immobile. As a result, substantial confinement of –SO_3^- and transport of H^+ ions achieve negative/positive charge separation to induce an electric field.

When a temperature difference occurs on the VHG, the H^+ ions will tend to diffuse from the hot side to the cold side for thermopower dominated by the Soret effect (Fig. 3(b)).[13] In addition, H^+ ion dissociation will be improved near the hot electrode.[36] The direction of thermodiffusion is in accord with the direction of vapor-induced H^+ ion migration (Fig. 3(c)). This alignment can achieve double-acting H^+ ion transport. Thus, the gradient distribution of H^+ ions induced by vapor adsorption could be further enhanced upon temperature difference, and H^+ ion thermodiffusion will be promoted by water adsorption accordingly.[34] The synergistic function of vapor and thermal gradient on VHG facilitates H^+ ion diffusion directionally for higher I_{sc}.

In addition to the thermal diffusion of ions, when a temperature gradient is built across the VHG, the balance of reversible reactions between the redox couple of $Fe(CN)_6^{4-}$ and $Fe(CN)_6^{3-}$ is broken, and the reversible reaction near the two electrodes will be inclined to the opposite direction.[47,62] In the ferri/ferrocyanide couple, the solvation entropy of $Fe(CN)_6^{4-}$ is lower than that of $Fe(CN)_6^{3-}$.[16] Specifically, the oxidation reaction $Fe(CN)_6^{4-} \rightarrow e^- + Fe(CN)_6^{3-}$ is favorable and releases electrons into the hot electrode, and then the electron through an external circuit is consumed at the cold cathode by the reduction of $Fe(CN)_6^{3-}$ to $Fe(CN)_6^{4-}$ (Fig. 3(c)). The oxidized species ($Fe(CN)_6^{3-}$) generated at the hot side and the reduced species ($Fe(CN)_6^{4-}$) generated at the cold side migrated to the other electrode under a concentration gradient, making continuous current output possible.[61] The thermogalvanic effect will generate a thermopower that is consistent with the diffusion contributions of H^+ ions. Consequently, the high power output of VHG under vapor and temperature difference is superior to electric performance induced by the individual factors (Fig. S17, ESI†), which confirms the synergy of the thermogalvanic effect of the redox couple $Fe(CN)_6^4/Fe(CN)_6^{3-}$, double-acting diffusion of H^+ ions.

This mechanism was further confirmed by experimental results and theoretical calculations. The mass change of VHG

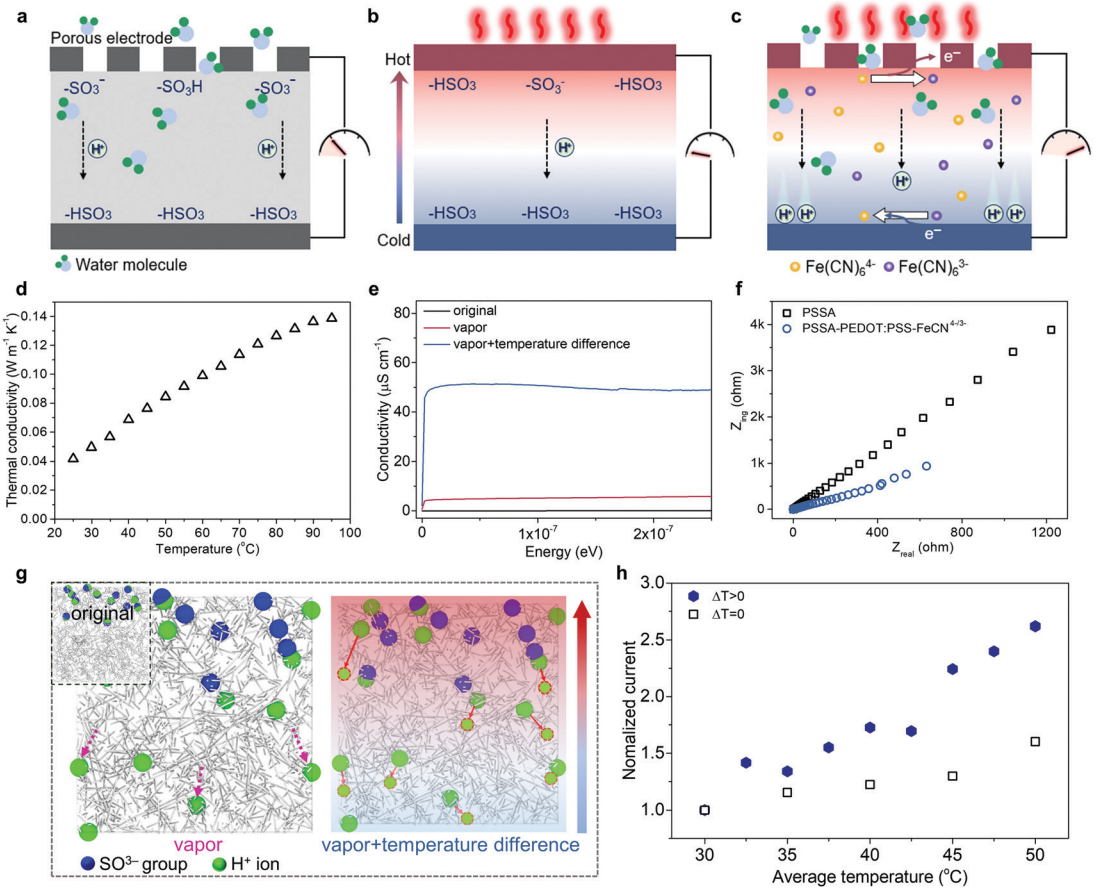

Fig. 3 Proposed mechanism of a VHG. (a) The functional groups in PSSA are ionized by incoming vapor and release H^+ ions to diffuse under vapor only. (b) When a temperature difference is applied on a VHG with excluded vapor absorption, H^+ ions will thermodiffuse from the hot side to the cold side. (c) Under vapor with temperature difference, H^+ ion diffusion is driven by water adsorption gradient and temperature gradient synergistically. Simultaneously, the reversible reaction of $Fe(CN)_6^{4-}$ and $Fe(CN)_6^{3-}$ redox couple occurs near the electrodes. (d) Thermal conductivity of PSSA-PEDOT:PSS-$FeCN^{4-/3-}$ film under RH = 70%. (e) The ionic conductivity of PSSA-PEDOT:PSS-$FeCN^{4-/3-}$ film under vapor (RH = 70%) and temperature difference (ΔT = 10 °C), respectively. (f) The electrochemical impedance of PSSA and PSSA-PEDOT:PSS-$FeCN^{4-/3-}$ film in response to vapor and temperature difference (RH = 70%, ΔT = 10 °C). (g) Simulation model snapshots: H^+ ions and negative $-SO^{3-}$ groups pairs distribution upon vapor (left) and vapor + temperature difference (right). (h) Temperature gradient influence on the calculated current with respect to the average temperature. For black dots, the temperatures at both ends were increased simultaneously; for blue dots, only the temperature at the top was changed. Note that the current of the sample was used to normalize the calculation results.

by water adsorption from air was about 150% at 70% RH (Fig. S18a, ESI†). In addition, a temperature difference of ~10 °C in VHG persisted during a long-term operation (Fig. S18b, ESI†). This results from the thermal conductivity of PSSA-PEDOT:PSS-$FeCN^{4-/3-}$ film being as low as 0.04 W m^{-1} K^{-1} at 298 K (Fig. 3(d) and Fig. S19, ESI†), allowing it to maintain a temperature gradient along the VHG for constant power generation.[44] Concurrently, induced electric power lasts more than 24 h (Fig. 1(c)). After water dehydration and cooling down, the reversible electricity generation of VHG can also be achieved by the subsequent water adsorption and heating again (Fig. S3, ESI†). When blocking the water adsorption and H^+ ion migration process under 0% RH and uniform temperature, VHG is unable to generate electricity owing to cutting off H^+ ion dissociation and diffusion (Fig. S20, ESI†). These results further validate that the spontaneous water adsorption and temperature gradient in VHG is the main reason for electricity generation. Notably, the general strategy is to use a negative temperature coefficient (*i.e.*, $a_R < 0$) and a p-type thermodiffusive thermopower (*i.e.*, Seebeck coefficient, $S_e > 0$) to generate a high thermopower.[16] The thermodiffusion of H^+ ions in PSSA-PEDOT:PSS film showed a p-type thermopower (Fig. S21, ESI†). The $Fe(CN)_6^{4}/Fe(CN)_6^{3-}$ redox couple has a negative temperature coefficient (Fig. S22 and S23, ESI†), along with vapor-induced electric field achieving a synergistic effect.

The ionic conductivity (σ) values of PSSA-PEDOT:PSS-$FeCN^{4-/3-}$ hybrids were obtained using electrochemical impedance spectroscopy (Fig. 3(e) and (f)). The σ of the original film was 0.04 μS cm^{-1}, which increased to 6.1 μS cm^{-1} upon RH = 70% (Fig. 3(e)). This strong σ dependency on water adsorption revealed that the spontaneous water absorption facilitated the dissociation and diffusion of H^+ ions under vapor, resulting in enhanced I_{sc}.[13] A further increasing trend was observed after

applying a temperature difference, which can be fitted into the following equation:

$$\sigma_T = \sigma_0 e^{-E_a/kT} \quad (1)$$

where σ_T is the ionic conductivity, k is the Boltzmann constant, T is the temperature, and σ_0 is the pre-exponential factor.[44] The σ of PSSA-PEDOT:PSS-FeCN$^{4-/3-}$ film increased to 51 μS cm^{-1} under temperature difference (Fig. 3(e)). In the ternary system of PSSA-PEDOT:PSS-FeCN$^{4-/3-}$ film, the higher conductivity suggested that H^+ ion migration was more efficient than that in simple components (Fig. 3(f), Fig. S24, ESI†).[36] Consequently, given different hydration levels between two sides of the PSSA-PEDOT:PSS-FeCN$^{4-/3-}$ film under vapor, the directional transport of H^+ ions will spontaneously realize charge separation and induce an electric output. This H^+ ion dissociation and migration induced by vapor will be further driven by the temperature gradient in VHG. Synchronously, water penetration under vapor could promote ion thermodiffusion. The increased carriers and abundant driving force for efficient H^+ ion diffusion work synergistically with the thermogalvanic effect of the redox couple, accordingly enhancing power generation as supported by the theoretical calculations.

To quantify the ion migration dependence of electricity generation, the kinetic Monte Carlo method (details in Supplementary note 1, ESI†) was used to study ion movement inside a polymer network. After the given directional vapor, positive/negative ion pairs were uncoupled, and hydrated H^+ ions diffused in the matrix. Note that negative groups were fixed and never diffused. After enough kinetic Monte Carlo timesteps, a built-in electric field was established, and the typical distribution of hydrated H^+ ions is shown in the left figure in Fig. 3(g). This H^+ ion migration was further improved under the temperature difference, presented in the red arrows of the right figure in Fig. 3(g).

As shown in Fig. 3(h), the remarkable current enhancement is closely related to the high temperature at the top. In Fig. 3(h), samples with a larger temperature difference ($\Delta T > 0$) produced a much higher current compared to the sample with uniform temperature ($\Delta T = 0$), which is comparable with the enhancement brought by the temperature difference in experiments (Fig. 2(e)). Therefore, this verifies that the temperature difference can further enhance the electric output of VHG. These theoretical calculation results further indicate the mechanism rationality of VHG. In addition, the variations in the chemical potential energy from gaseous water in air to the adsorbed water in the device and heat input power are the main input energy sources in this process of electricity generation in VHG. The energy conversion efficiency was estimated to be about 1.7% (Supplementary note 3, ESI†).

Scalable integration of VHGs

The scalable integration of electric generators is critical for realizing highly efficient power output in the ambient environment. The output voltage could be enhanced by proper connection. For example, 6.7 V voltage can be easily reached by connecting six VHG units in series (Fig. 4(a)). Notably, the area of the PSSA-PEDOT:PSS-FeCN$^{4-/3-}$ film varied, ranging from 0.25 cm^2 to 25 cm^2. By enlarging the device area, a 25 cm^2 unit can achieve a stable current of 1.7 mA and a voltage of 0.82 V (Fig. 4(b) and (c)). Moreover, the addition of PEDOT:PSS-FeCN$^{4-/3-}$ could potentially improve the stretchability owing to the hard and stiff nature

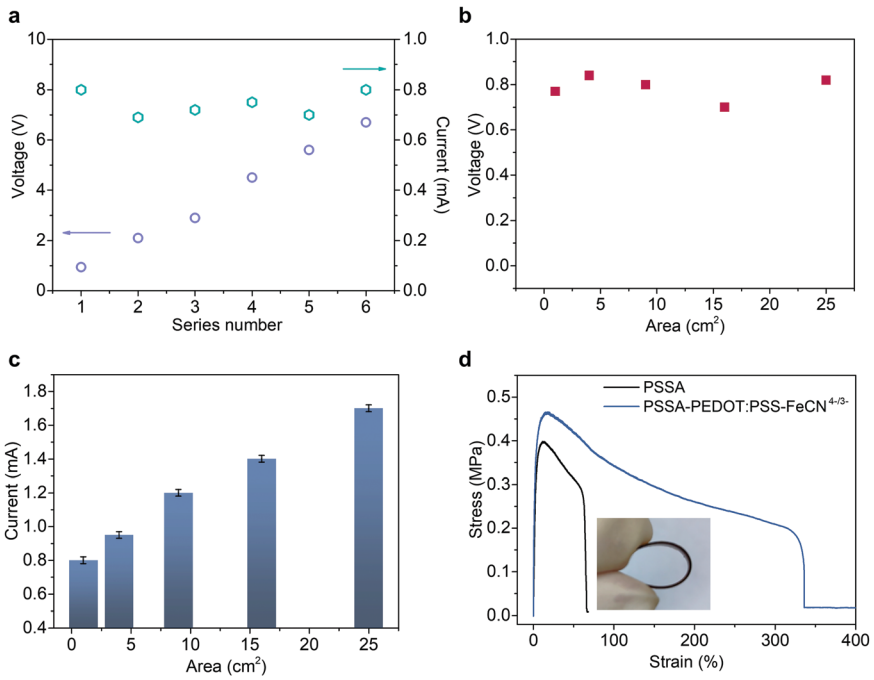

Fig. 4 Performance of integrated VHGs. (a) The V_{oc} output of 0.25 cm^2 VHG units connected in series. (b) V_{oc} and (c) current output of one VHG unit with different area. The testing conditions were 70% RH, and ΔT = 10 °C. (d) Stress–strain curves of PSSA and PSSA-PEDOT:PSS-FeCN$^{4-/3-}$ film. Inset: Photograph of the PSSA-PEDOT:PSS-FeCN$^{4-/3-}$ film in the bending state.

of the inorganic $FeCN^{4-/3-}$ and hydrogen bonds between the components.[39] The hybrid film displayed mechanical strength with an elastic strain of about 19.0%, a modulus of about 0.5 MPa, as compared with an elastic strain of about 12.7%, and a modulus of about 0.4 MPa for the PSSA film (Fig. 4(d)). Due to the pliant nature of the composite film (insert of Fig. 4(d)), flexible VHGs can be conveniently fabricated. These considerable power outputs and endurance for mechanical deformations make them practicable to integrate VHGs for scalable applications under different natural environments without temporal and geographical limitations.

To demonstrate the practical applicability, an integrated module was fabricated by connecting VHG units in a series-parallel connection. The electricity generated by VHG can be directly utilized or stored in commercial energy-storage devices without an extra rectifier (Fig. S25, ESI†). Capacitors with 25 μF–5 F could be charged to 5–10 V (Fig. S26, ESI†). Natural vapor and temperature differences are ubiquitous, providing opportunities for the actual performance of power-supplying systems in real conditions. VHGs can produce considerable electric output for powering commercial appliances by spontaneously adsorbing water in air and harvesting low-grade thermal sources over a wide range of temperatures (10–80 °C) and humidity (20–90%), adapting to most of the environmental scenarios and seasons across the earth.

From July to November of 2021, we tested the power generation performance of integrated VHGs on the campus of Tsinghua University, Beijing. Particularly, a prototype containing 15 VHG units (0.25 cm^2) was attached to the outer wall of a cup as illustrated in Fig. 5(a). In the hot summer (Beijing, China, July to August 2021), the bottom sides of VHGs were cooled down by ice water (4 °C) in the cup, while the upper side of VHGs was warmed at the ambient temperature of 30 °C. The natural temperature gradient established along the VHGs (ΔT = 10 °C) together with natural moist air (RH = 72%) near the cup provided an appropriate environment for VHGs. The electric output of VHG can be stored in a capacitor, and the accumulated electric energy powered an electric fan for human comfort (Fig. 5(b), (c) and Video S1, ESI†). In addition, scalable VHG devices can be reconfigured in series in the shadow of a tree, the power generated under ambient conditions directly drives fancy lanterns adorned on the tree trunk (Fig. 5(d) and (e)). A similar module can also work by floating on the lake surface (Fig. 5(f)). The upper porous electrodes were painted black for the higher temperature of 36 °C and the bottom electrode adhered to a white substrate near the lake surface with a lower temperature of 28 °C (ΔT = 8 °C, RH = 60–70%). VHGs can provide enough power to directly run a model lighthouse (Fig. 5(g)).

The highly flexible VHGs are also suitable for wearable systems. Human bodies are natural sources of constant humidity and heat, which have great potential for powering commercial electronics by collectively utilizing the sweat of human skin and the temperature difference between human bodies and the outer environment (Fig. 6(a)). For example, when the VHGs on a flexible PET substrate are around the wrist, it generates V_{oc} of about 3.6 V

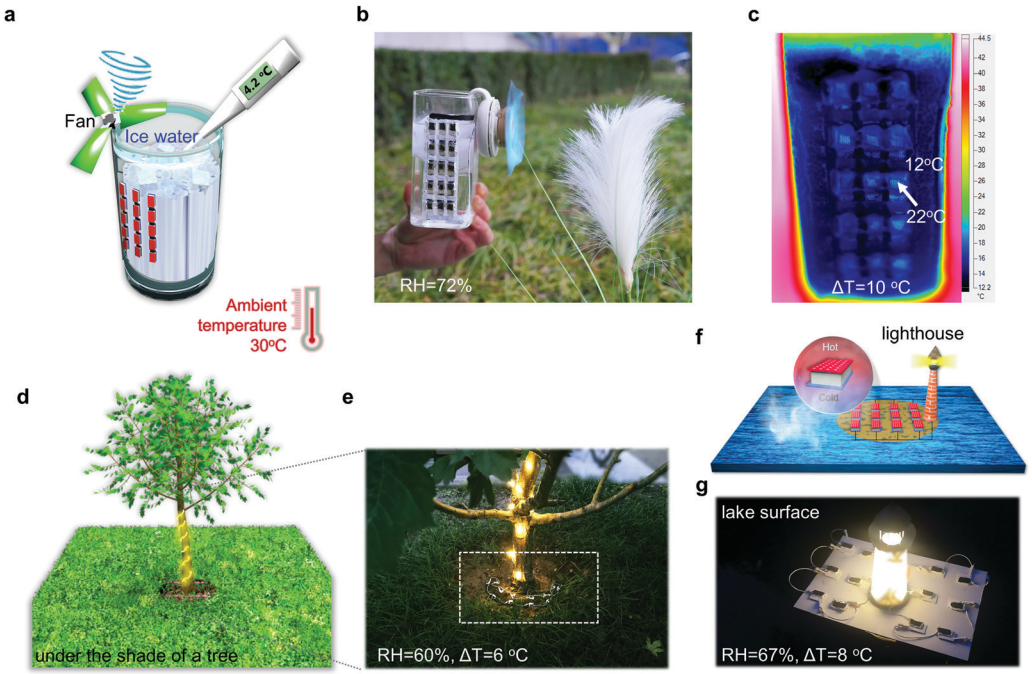

Fig. 5 Demonstration of VHGs as practical power sources in real life conditions of summer (Beijing, China, July to August, 2021). (a) Schematic diagram of integrated VHGs on the outer wall of a glass cup filled with ice water. (b) Photograph of VHGs running an electric fan smoothly. (c) The infra-red image showing real temperature of VHGs on the outer wall of the glass cup. The ambient temperature is 30 °C and the temperature of ice water is 4.2 °C. (d) Schematic diagram and (e) photograph of VHGs fastened in the shadow of a tree. Fancy lanterns adorned on the tree trunk are lighted by serially connected VHGs directly. (f) Schematic diagram and (g) photograph of VHGs floating on the lake to power a lighthouse model. These images were obtained in real natural environments without any other auxiliaries.

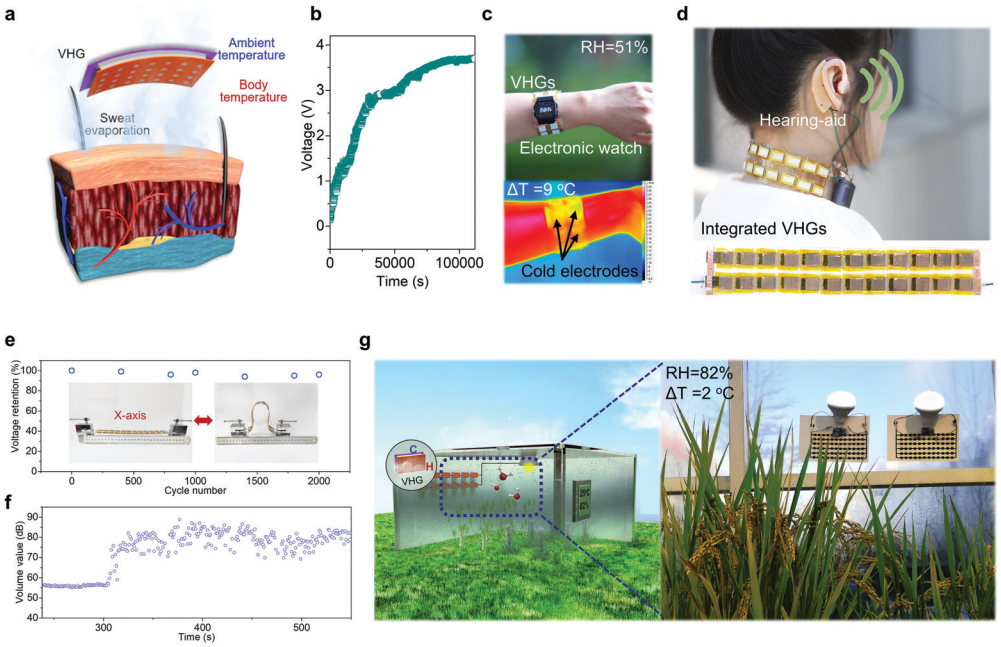

Fig. 6 Demonstration of VHG as a practical power source in real life conditions of winter (Beijing, China, October to November, 2021). (a) Schematic diagram of a VHG adhered to human skin. (b) V_{oc} generated from VHGs worn on the human wrist. (c) Photograph and IR image of a self-powered electronic watch under working conditions. The surface temperature of the human arm was 26.0 °C and the temperature of electrodes exposed to air was 17.1 °C. (d) The VHGs bent around the neck of a human can power a hearing-aid. Inset: Photograph of integrated VHGs. (e) Voltage retention of VHGs after various bending cycles. Inset: Photograph of integrated VHGs from the original state to the bending state. (f) Volume monitored by a decibel meter before and after the hearing-aid run by VHGs. (g) VHGs installed on the inner wall of a greenhouse. The outdoor temperature was 13 °C, and the indoor temperature in the greenhouse was 25 °C.

(Fig. 6(b)) at the natural RH of 51%, and ΔT of 8.9 °C near human skin. This power can directly run an electronic watch (Fig. 6(c) and Fig. S27, ESI†). A similar module assembled by connecting 24 VHG units presents good mechanical flexibility. The V_{oc} was stably maintained even after 2000 bending cycles. A "necklace" consisting of VHGs can be easily bent to be worn on the human neck (Fig. 6(d) and (e) and Fig. S28, ESI†). The power generated by this wearable power-supplying system is enough to charge a capacitor for driving a hearing aid (Fig. 6(f)). The personally wearable VHG can fully harvest natural vapor and heat from the human body and thus power compact applications to authentically meet human needs.

Furthermore, the natural vapor and temperature difference also exist in the scenario of agriculture. In a greenhouse with RH of 82%, when VHG units assemble on the inner wall, adequate vapor and temperature differences between the indoor temperature of 25 °C and outdoor temperature of 13 °C can make VHGs achieve electric output. The accumulated energy is enough to power a lamp bulb of 15 Watt (Fig. 6(g)). These examples show that VHG could be a viable technology for spontaneously utilizing the multiple natural energies of vapor and low-grade heat from outdoor environments and organisms for powering electricity-consuming devices in various scenarios of daily life, horticultural decoration and agriculture.

Conclusions

In summary, we have developed a VHG for spontaneously adsorbing vapor and harvesting concomitant heat from the natural environment. This VHG dual-driven by vapor and heat can deliver a voltage output of 0.94 V and a considerable current density of up to 0.8 mA cm^{-2}. The high-performance power generation is attributed to the synergistic combination of vapor and thermal-gradient function in the redox-involved polyelectrolyte composites, where hydrophilic polyelectrolyte plays a role in vapor-induced ion migration and thermodiffusion, and a redox couple is introduced for thermogalvanic effects. This was confirmed by experimental results and kinetic Monte Carlo simulations. VHG is applicable in most scenarios of human activity over a wide range of temperatures (10–80 °C) and RH (30–90%), regardless of weather and geographical conditions. The flexible and tailorable VHGs can not only spontaneously power portable electronics but also work as personal energy supply systems to power wearable and portable devices for applications in daily life by fully harvesting body sweat and heat. Furthermore, such integrated VHGs can be employed for horticultural decoration and agriculture in various seasons. For practical applications, VHGs will work under various natural conditions with various RH, temperature, light intensity, and wind speed. The combination techniques of VHGs with some energy storage devices and controller modules, such as capacitors, rectifiers, chips, will be well developed to ensure stable power output during long-term operation in complex and mutable environments. The self-powered energy supplies through the comprehensive utilization of natural sources in a multi-drive system from ambient environments have the potential to serve the Internet of Things and Smart Life systems in the future.

Experimental section

Materials

The raw materials, namely, poly(4-styrenesulfonic acid) (PSSA) solution (M_w 75 000, 30 wt% in H_2O, Alfa Aesar). Poly(3,4-ethylenedioxythiophene)-poly(styrenesulfonate) (PEDOT:PSS), CLEVIOS™ P VP AI 4083, from Heraeus. $K_3Fe(CN)_6$ (M_W = 329.26, ≥98%) and $K_4Fe(CN)_6{\cdot}3H_2O$ (M_W = 422.39, ≥98%), were purchased from Alfa Aesar. All chemical reagents were employed without further purification.

Preparation of PSSA-PEDOT:PSS-FeCN$^{4-/3-}$ film

PEDOT:PSS and $K_4Fe(CN)_6/K_3Fe(CN)_6$ were mixed with an aqueous PSSA solution. The mixed solution was cast into a mold and dried overnight in an oven at 37 °C and RH was set to 45%. The hybrid film was obtained at a ratio of PSSA (92 wt%):PEDOT:PSS (7 wt%):$K_4Fe(CN)_6/K_3Fe(CN)_6$ (1 wt%). Similarly, PSSA-PEI, PSSA-rGO, PSSA-Ppy, PSSA-cellulose, PSSA-gelatin, PSSA-PEDOT:PSS-Co II/III, PSSA-PEDOT:PSS-I^-/I_3^-, PSSA-PEDOT:PSS-CNTs, PSSA-PEDOT:PSS-SiO_2 nanoparticles films could be prepared by the same protocol as PSSA-PEDOT:PSS-FeCN$^{4-/3-}$ film.

Preparation of electrodes

Uniformly distributed holes were manufactured on the upper electrode for ventilation. The diameter of the holes was 1.3 mm. A pair of graphite electrodes were applied in tests in Fig. 1–4 and Fig. S1–S30 (ESI†), except for Fig. S7 (ESI†). In Fig. 5 and 6, PET pre-printed with carbon paste served as electrodes in the flexible VHG. In Fig. S7 (ESI†), carbon paper, carbon tape, Au, Ag and Pt were used as electrodes.

Fabrication of VHG

The obtained PSSA-PEDOT:PSS-FeCN$^{4-/3-}$ film was sandwiched between two electrodes and inserted into a test circuit in an enclosed container with an RH and temperature controlling system for electrical measurements. The polyacrylonitrile-based carbon fibers were adhered to the upper electrode to heat. The real-time temperature of VHG was monitored by a multichannel thermocouple thermometer (Apllent, AT4516) *in situ*.

Electric measurement

All the voltage and current signals were recorded by a Keithley 2400 multimeter, which was controlled by a LabView-based data acquisition system. The circuit parameters of the V_{oc} test were current = 0 mA and step index = 10 points s^{-1}. The circuit parameters of the I_{sc} test were voltage = 0 V and step index = 10 points s^{-1}. The electrochemical tests were conducted on a PARSTAT 3000A electrochemical workstation.

Material characterization

The morphology and microstructures of films were characterized using a Sirion-200 field-emission scanning electron microscope (FEI Corporation, USA). Fourier Transform infrared spectroscopic (FTIR) tests were conducted on a Nicolet 6700FTIR. The temperature distributions of devices were recorded by an IR camera (Fluke). Thermogravimetry Analysis spectra were obtained from TA INSTRUMENTS, Q5000IR. The mechanic tensile tests were conducted by an Instron 5943 universal testing machine. The freestanding samples were held by a pneumatic grip, and the gauge length was set to ~20 mm with a stretching rate of 10 mm min^{-1}. Volume was monitored by a decibel meter (Aicevoos, 0.1 dB).

Thermal conductivity measurement

The thermal conductivity (k) was calculated from the equation $k = C_p\rho D$, where C_p is the specific heat capacity, ρ is the density of the sample, and D is the thermal diffusivity. Thermal diffusivity was conducted on a laser flash analysis (LFA 447). The thermal diffusivity is described by $D = 0.1388\ d^2/t_{1/2}$, where d is the thickness of the sample, and $t_{1/2}$ is the time to reach the half-maximum temperature. The specific heat capacity was obtained using differential scanning calorimetry (DSC, Q5000IR).

The ionic electrical conductivity measurement

The ionic conductivities of the sample films were measured by broadband dielectric impedance spectrometer (CONCEPT-80, NOVOCONTROT) in the frequency range from 0.8 MHz to 0.1 Hz. The concrete value in conductivity is determined by

$$\sigma = \frac{L}{R \times S} \tag{2}$$

where σ: ionic conductivity, L: thickness, S: electrode area and R: ($Z_{real}/|Z|$).

Author contributions

L. Q. and J. B. designed the experiments. J. B., T. G. and K. Z. performed the experiments. Y. H. and F. L. conducted the computational studies. J. B. designed and characterized the VHG. H. W., H. C. and Q. L. gave advice on experiments. All authors discussed the results and reviewed the manuscript. L. Q. supervised the entire project.

Conflicts of interest

There are no conflicts to declare.

Acknowledgements

This work was supported by the financial support from the National Science Foundation of China (No. 22035005, 52022051, 22075165, 52073159, 52090032, 11972349, 11790292), State Key Laboratory of Tribology (SKLT2021B03), Tsinghua-Foshan Innovation Special Fund (2020THFS0501), the Strategic Priority Research Program of the Chinese Academy of Sciences (Grant No. XDB22040503). This work was also supported by Scientific Research Project of Beijing Educational Committee (KZ202110017026) and a grant (2019GQG1025) from the Institute for Guo Qiang, Tsinghua University.

References

1 X. Pu, L. Li, H. Song, C. Du, Z. Zhao, C. Jiang, G. Cao, W. Hu and Z. Wang, *Adv. Mater.*, 2015, **27**, 2472–2478.
2 W. Li, L. Ye, S. Li, H. Yao, H. Ade and J. Hou, *Adv. Mater.*, 2018, **30**, 1707170.
3 F. P. G. Márquez, A. M. Tobias, J. M. P. Pérez and M. Papaelias, *Renewable Energy*, 2012, **46**, 169–178.
4 Y. Zi, J. Wang, S. Wang, S. Li, Z. Wen, H. Guo and Z. Wang, *Nat. Commun.*, 2016, **7**, 10987.
5 L. Wang and J. Song, *Science*, 2006, **312**, 242–246.
6 M. Mohammadifar, M. Tahernia, J. Yang, A. Koh and S. Choi, *Nano Energy*, 2020, **75**, 104994.
7 W. G. Zeier, A. Zevalkink, Z. M. Gibbs, G. Hautier, M. G. Kanatzidis and G. J. Snyder, *Angew. Chem., Int. Ed.*, 2016, **55**, 6826–6841.
8 J. He and T. M. Tritt, *Science*, 2017, **357**, 1369.
9 Y. Huang, H. Cheng, C. Yang, P. Zhang, Q. Liao, H. Yao, G. Shi and L. Qu, *Nat. Commun.*, 2018, **9**, 4166.
10 F. Zhao, Y. Liang, H. Cheng, L. Jiang and L. Qu, *Energy Environ. Sci.*, 2016, **9**, 912–916.
11 M. Li, L. Zong, W. Yang, X. Li, J. You, X. Wu, Z. Li and C. Li, *Adv. Funct. Mater.*, 2019, **29**, 1901798.
12 S. Hong, G. Zou, H. Kim, D. Huang, P. Wang and H. N. Alshareef, *ACS Nano*, 2020, **14**, 9042–9049.
13 D. Zhao, H. Wang, Z. U. Khan, J. C. Chen, R. Gabrielsson, M. P. Jonsson, M. Berggrena and X. Crispin, *Energy Environ. Sci.*, 2016, **9**, 1450–1457.
14 J. Bai, Y. Huang, H. Wang, T. Guang, Q. Liao, H. Cheng, S. Deng, Q. Li, Z. Shuai and L. Qu, *Adv. Mater.*, 2022, **34**, 2103897.
15 B. Kim, J. U. Hwang and E. Kim, *Energy Environ. Sci.*, 2020, **13**, 859–867.
16 C. Han, X. Qian, Q. Li, B. Deng, Y. Zhu, Z. Han, W. Zhang, W. Wang, S. Feng, G. Chen and W. Liu, *Science*, 2020, **368**, 1091–1098.
17 F. Zhao, H. Cheng, Z. Zhang, L. Jiang and L. Qu, *Adv. Mater.*, 2015, **27**, 4351–4357.
18 H. Cheng, Y. Huang, F. Zhao, C. Yang, P. Zhang, L. Jiang, G. Shi and L. Qu, *Energy Environ. Sci.*, 2018, **11**, 2839–2845.
19 Y. Liang, F. Zhao, Z. Cheng, Y. Deng, Y. Xiao, H. Cheng, P. Zhang, Y. Huang, H. Shao and L. Qu, *Energy Environ. Sci.*, 2018, **11**, 1730–1735.
20 C. Shao, J. Gao, T. Xu, B. Ji, Y. Xiao, C. Gao, Y. Zhao and L. Qu, *Nano Energy*, 2018, **53**, 698–705.
21 Y. Huang, H. Cheng, C. Yang, H. Yao, C. Li and L. Qu, *Energy Environ. Sci.*, 2019, **12**, 1848–1856.
22 T. Xu, X. Ding, C. Shao, L. Song, T. Lin, X. Gao, J. Xue, Z. Zhang and L. Qu, *Small*, 2018, **14**, 1704473.
23 C. Yang, Y. Huang, H. Cheng, L. Jiang and L. Qu, *Adv. Mater.*, 2019, **31**, 1805705.
24 K. Liu, P. Yang, S. Li, J. Li, T. Ding, G. Xue, Q. Chen, G. Feng and J. Zhou, *Angew. Chem., Int. Ed.*, 2016, **55**, 8003–8007.
25 J. Xue, F. Zhao, C. Hu, Y. Zhao, H. Luo, L. Dai and L. Qu, *Adv. Funct. Mater.*, 2016, **26**, 8784–8792.
26 X. Nie, B. Ji, N. Chen, Y. Liang, Q. Han and L. Qu, *Nano Energy*, 2018, **46**, 297–304.
27 D. Shen, M. Xiao, G. Zou, L. Liu, W. W. Duley and Y. Zhou, *Adv. Mater.*, 2018, **30**, 1705925.
28 H. Wang, Y. Sun, T. He, Y. Huang, H. Cheng, C. Li, D. Xie, P. Yang, Y. Zhang and L. Qu, *Nat. Nanotechnol.*, 2021, **16**, 811–819.
29 T. Xu, X. Ding, Y. Huang, C. Shao, L. Song, X. Gao, Z. Zhang and L. Qu, *Energy Environ. Sci.*, 2019, **12**, 972–978.
30 Z. Luo, C. Liu and S. Fan, *Nano Energy*, 2019, **60**, 371–376.
31 H. Wang, H. Cheng, Y. Huang, C. Yang, D. Wang, C. Li and L. Qu, *Nano Energy*, 2020, **67**, 104238.
32 R. Zhu, Y. Zhu, F. Chen, R. Patterson, Y. Zhou, T. Wan, L. Hu, T. Wu, R. Joshi, M. Li, C. Cazorla, Y. Lu, Z. Han and D. Chu, *Nano Energy*, 2022, **94**, 106942.
33 J. Eun and S. Jeon, *Nano Energy*, 2022, **92**, 106772.
34 Z. A. Akbar, J. W. Jeon and S. Y. Jang, *Energy Environ. Sci.*, 2020, **13**, 2915–2923.
35 S. Sengupta and A. V. Lyulin, *J. Phys. Chem. B*, 2019, **123**, 6882–6891.
36 M. Jeong, J. Noh, M. Z. Islam, K. Kim, A. Sohn, W. Kim and C. Yu, *Adv. Funct. Mater.*, 2021, **31**, 2011016.
37 B. Kim, J. Na, H. Lim, Y. Kim, J. Kim and E. Kim, *Adv. Funct. Mater.*, 2019, **29**, 1807549.
38 G. Li, D. Dong, G. Hong, L. Yan, X. Zhang and W. Song, *Adv. Mater.*, 2019, **31**, 1901403.
39 Y. T. Malik, Z. A. Akbar, J. Y. Seo, S. Cho, S. Y. Jang and J. W. Jeon, *Adv. Energy Mater.*, 2021, **12**, 2103070.
40 H. Zhou, T. Yamada and N. Kimizuka, *J. Am. Chem. Soc.*, 2016, **138**, 10502–10507.
41 P. F. Salazar, S. T. Stephens, A. H. Kazim, J. M. Pringle and B. A. Cola, *J. Mater. Chem. A*, 2014, **2**, 20676–20682.
42 M. A. Lazar, D. Al-Masri, D. R. MacFarlane and J. M. Pringle, *Phys. Chem. Chem. Phys.*, 2016, **18**, 1404–1410.
43 M. S. Romano, N. Li, D. Antiohos, J. M. Razal, A. Nattestad, S. Beirne, S. Fang, Y. Chen, R. Jalili, G. G. Wallace, R. Baughman and J. Chen, *Adv. Mater.*, 2013, **25**, 6602–6606.
44 T. Li, X. Zhang, S. D. Lacey, R. Mi, X. Zhao, F. Jiang, J. Song, Z. Liu, G. Chen, J. Dai, Y. Yao, S. Das, R. Yang, R. M. Briber and L. Hu, *Nat. Mater.*, 2019, **18**, 608–613.
45 H. Cheng, Y. Huang, L. Qu, Q. Cheng, G. Shi and J. Lan, *Nano Energy*, 2017, **45**, 37–43.
46 W. Zhao, F. Zhang, X. Dai, W. Jin, L. Xiang, J. Ding, X. Wang, Y. Wan, H. Shen, Z. He, J. Wang, X. Gao, Y. Zou, C. A. Di and D. Zhu, *Adv. Mater.*, 2020, **32**, 2000273.
47 B. Yu, J. Duan, H. Cong, W. Xie, R. Liu, X. Zhuang, H. Wang, B. Qi, M. Xu, Z. Wang and J. Zhou, *Science*, 2020, **370**, 342–346.
48 J. Duan, G. Feng, B. Yu, J. Li, M. Chen, P. Yang, J. Feng, K. Liu and J. Zhou, *Nat. Commun.*, 2018, **9**, 5146.
49 K. Kim and H. Lee, *Phys. Chem. Chem. Phys.*, 2018, **20**, 23433–23440.
50 T. Kang, S. Fang, M. E. Kozlov, C. S. Haines, N. Li, Y. Kim, Y. Chen and R. H. Baughman, *Adv. Funct. Mater.*, 2012, **22**, 477–489.
51 L. Zhang, T. Kim, N. Li, T. Kang, J. Chen, J. M. Pringle, M. Zhang, A. H. Kazim, S. Fang, C. Haines, D. Al-Masri, B. A. Cola, J. M. Razal, J. Di, S. Beirne, D. R. MacFarlane, A. G. Martin, S. Mathew, Y. Kim, G. Wallace and R. H. Baughman, *Adv. Mater.*, 2017, **29**, 1605652.

52 O. Bubnova, Z. U. Khan, A. Malti, S. Braun, M. Fahlman, M. Berggren and X. Crispin, *Nat. Mater.*, 2011, **10**, 429–433.
53 G. Kim, L. Shao, K. Zhang and K. P. Pipe, *Nat. Mater.*, 2013, **12**, 719–723.
54 P. Yang, K. Liu, Q. Chen, X. Mo, Y. Zhou, S. Li, G. Feng and J. Zhou, *Angew. Chem., Int. Ed.*, 2016, **128**, 12229–12232.
55 J. Duan, B. Yu, K. Liu, J. Li, P. Yang, W. Xie, G. Xue, R. Liu, H. Wang and J. Zhou, *Nano Energy*, 2019, **57**, 473–479.
56 D. Zhao, A. Martinelli, A. Willfahrt, T. Fischer, D. Bernin, Z. U. Khan, M. Shahi, J. Brill, M. P. Jonsson, S. Fabiano and X. Crispin, *Nat. Commun.*, 2019, **10**, 1093.
57 T. Kim, J. Lee, G. Lee, H. Yoon, J. Yoon, T. Kang and Y. Kim, *Nano Energy*, 2017, **31**, 160–167.
58 L. Jin, G. W. Greene, D. R. MacFarlane and J. M. Pringle, *ACS Energy Lett.*, 2016, **1**, 654–658.
59 N. Komatsu, Y. Ichinose, O. S. Dewey, L. W. Taylor, M. A. Trafford, Y. Yomogida, G. Wehmeyer, M. Pasquali, K. Yanagi and J. Kono, *Nat. Commun.*, 2021, **12**, 4931.
60 H. Im, T. Kim, H. Song, J. Choi, J. Park, R. O. Robles, H. Yang, K. D. Kihm, R. H. Baughman, H. Lee, T. Kang and Y. Kim, *Nat. Commun.*, 2016, **7**, 10600.
61 R. Hu, B. A. Cola, N. Haram, J. N. Barisci, S. Lee, S. Stoughton, G. Wallace, C. Too, M. Thomas, A. Gestos, M. E. dela Cruz, J. P. Ferraris, A. A. Zakhidov and R. H. Baughman, *Nano Lett.*, 2010, **10**, 838–846.
62 H. G. Hertz and S. K. Ratkje, *J. Electrochem. Soc.*, 1989, **136**, 1698–1740.

